Homoclinic chaos in the rf superconducting quantum-interference device

W. C. Schieve*
Max-Planck-Institut fur Quantenoptik, Garching, Federal Republic of Germany and Naval Ocean Systems Center, Research Branch, San Diego, California 92152

A. R. Bulsara and E. W. Jacobs
Naval Ocean Systems Center, Research Branch, San Diego, California 92152
(Received 24 August 1987; revised manuscript received 30 November 1987)

We consider a simple model of the flux in a rf superconducting quantum-interference device (SQUID) ring subjected to an external periodic magnetic field. The dynamic equation describing the flux response of the SQUID is solved analytically in the absence of damping and external driving terms. We then introduce these terms as small perturbations, and construct, for this system, the Melnikov function, the zeros of which indicate the onset of homoclinic behavior. For the parameter values under consideration, excellent agreement is obtained between our theoretical predictions and numerical calculations of the stable and unstable (i.e., time-reversed) solution manifolds. A chaotic attractor is shown to appear somewhat above the homoclinic threshold.

I. INTRODUCTION

In this paper we wish to consider the appearance of homoclinic instabilities and chaos in the driven rf SQUID (superconducting quantum-interference device). Since Poincaré,[1] it has been known that under perturbation, the stable and unstable manifolds emanating from a hyperbolic fixed point are no longer identical and may cross, giving rise to an infinite number of intersections (homoclinic points), the resulting motion being so complicated that it may be characterized as chaotic (or statistical). An existence theorem of Smale and Moser[2] states that the motion in a region near a homoclinic point is homeomorphic to a Markov shift map. Thus, in this region, the test of the wild instability of the motion is the presence of homoclinic crossing. Since the separatrix solutions are so sensitive to perturbation, a simple theoretical test function due to Melnikov[3-6] may be used to determine the presence of the homoclinic instability.

This simple theoretical analysis has been applied to a number of driven oscillators[4,5] and, in particular to the rf-driven Josephson junction,[7-11] which constitutes the primary element of the rf SQUID under consideration in this work. The mechanical analog to the Josephson junction is a driven damped pendulum which is well known, numerically, to exhibit chaos and a "strange" attracting set. Both the unperturbed Josephson junction and the rf SQUID are *multistable* systems. In particular, the rf SQUID exhibits hysteresis above a certain threshold value of a characteristic parameter [the response of the device below its hysteretic threshold to a general perturbation of dc, random, and periodic components has been studied by one of the authors[12] (A.R.B.)]. In this work we shall concern ourselves with the operation of the rf SQUID in the hysteretic regime. Far fewer studies concerning the appearance of chaos have been done on the rf SQUID than in the Josephson junction (for a review of the latter, see Ref. 8). Dmitrenko *et al.*[13] report an experimental broadband amplitude spectrum in the hysteretic regime. Smith *et al.*[14] report on the results of numerical simulations suggesting period doubling to chaos and qualitative agreement with experiment. Finally, Ritala and Salomaa[15] have observed the transition from quasiperiodicity to chaos via the Feigenbaum period-doubling scenario for the case of the sinusoidally driven rf SQUID. Their work represents a major step forward in our understanding of the nonlinear dynamics associated with this system. It is our object in this work to theoretically predict the onset of homoclinic instability by means of the Melnikov test function, and then to compare this result with a numerical calculation of the manifold crossing. This latter has not been done for even the rf-driven Josephson junction. Comments are also made concerning the appearance of a strange attractor in the rf SQUID above its homoclinic threshold.

In its simplest form, the rf SQUID consists of a single Josephson junction shorted by a superconducting loop having an inductance L. An external magnetic field produces a geometrical flux Φ_e in the loop together with a circulating supercurrent $i(t)=-I_1\sin(2\pi\Phi/\Phi_0)$, where $\Phi=\Phi_e+Li$ is the actual flux sensed by the loop in the steady state, Φ_0 being the flux quantum ($\Phi_0\equiv h/2e=2.07\times10^{-15}$ Wb). The flux Φ in the SQUID ring obeys the dynamical equation[16]

$$\frac{\ddot{x}}{\omega_0^2}+\tau_L\dot{x}+x+\frac{\beta_e}{2\pi}\sin(2\pi x)=x_e\ , \tag{1.1}$$

where the sinusoidal contribution arises from the Josephson screening current. Here, the dot denotes the time derivative, $x\equiv\Phi/\Phi_0$, $x_e\equiv\Phi_e/\Phi_0$, $\omega_0^2\equiv 1/LC$, $\tau_L\equiv L/R$, and $\beta_e\equiv 2\pi LI_1/\Phi_0$. C and R are the capacitance and normal-state resistance of the loop, I_1 being the junction critical current. It is worth pointing out that the quantity $(\beta_e/2\pi)\omega_0^2$ is simply the plasma frequency ω_J^2 of the

junction; ω_J is the frequency of low-amplitude solutions of the Josephson-junction equations in the absence of an external magnetic flux. The parameter $\beta \equiv \beta_e/2\pi$ determines the hysteric threshold of the SQUID; above a critical value $\beta \equiv \beta_c$, the solutions of x of (1.1) are multivalued. For the undriven (autonomous) rf SQUID with negligible damping, one may case (1.1) in the form

$$\ddot{z} = -\frac{dU}{dz} , \tag{1.2}$$

where the potential $U(z)$ is given by

$$U(z) = \frac{\omega_0^2}{2}\left[z + \frac{\pi}{2} - 2\pi x_0\right]^2 + 2\pi\beta\omega_0^2 \sin z . \tag{1.3}$$

Here, for later convenience, we have made the phase transformation $z = 2\pi x - (\pi/2)$, $x_e \equiv x_0$ being an external (background) dc signal. One may readily verify via simple graphical analyses that, for $x_0 = 0, 1, 2, \ldots$, one obtains multivalued solutions to (1.1) above a critical value $\beta_e \approx 0.7325$. For the cases $x_0 = \frac{1}{2}, \frac{3}{2}, \frac{5}{2} \ldots$ one obtains $\beta_c \equiv (2\pi)^{-1}$. For any other value of x_0, the critical nonlinearity parameter β_c lies between the two limiting values given above. Throughout this work we shall set the dc driving term x_0 equal to zero; the potential (1.3) is then symmetric about $z = -\pi/2$. This potential has been plotted in Fig. 1 for $\beta = 2$ and $\omega_0 = 1$. In the later sections we will include a damping force

$$F_k = -k\dot{z}(t) , \tag{1.4}$$

and a periodic driving force

$$x_e \equiv F_\omega = A \sin[\omega(t - t_0)] , \tag{1.5}$$

in (1.2).

It is apparent from the potential, Fig. 1, that z_1 and z_3 are unstable hyperbolic fixed points and that five elliptic fixed points occur (for the range of z values used in this figure in general, one expects an infinite number of fixed points). In this work we will focus on the separatrix energy $U(z_1) = U(z_2) = U(z_3) = U(z_4)$ and thus be primarily concerned with the region of the two lowest-lying hyperbolic fixed points. The steady solutions to Eq. (1.2) are given by

$$0 = -\left[z_s + \frac{\pi}{2}\right] - 2\pi\beta \cos z_s . \tag{1.6}$$

Simple graphical analysis shows that for $\beta \approx 0.7325$ a new fixed point (other than $z_s = -\pi/2$) appears at $z_s = \pi$. For $\beta > 0.7325$ multistability occurs (as pointed out earlier). The character of these new fixed points may be analyzed by linear stability analysis with the eigenvalues λ of the linearized equations determined in the familiar fashion.[5] We find

$$\lambda = \pm\omega_0(1 - 2\pi\beta \sin z_s)^{1/2} , \tag{1.7}$$

from which it may be seen, for $\beta > \beta_c \approx 0.7325$, that the new fixed points appear (symmetric about $z_s = -\pi/2$) in "pairs" of hyperbolic and elliptic points, as indicated by the potential in Fig. 1. It may be shown that the hyperbolic point z_1 in Fig. 1 lies in the range $\pi/2 \le z_1 \le \pi$. An interesting feature of this system is the growth of the side wells of the potential as the nonlinearity β is increased. This feature is not present in the Josephson junction, where all peaks and wells of the potential are equal.

In Sec. II we will consider the time-dependent analytic solution of (1.2) on the separatrix. This is accomplished via a spline polynomial approximation of the nonlinear term in (1.2), a procedure that will be discussed in some detail. This method has also been carried through for the off-separatrix solution and is discussed briefly in this section. In Sec. III we apply this solution to the calculation of the Melnikov test function for the rf SQUID for the center as well as the side wells of Fig. 1. In this section we also numerically search for the homoclinic points and Cantor set structure predicted by the Melnikov function, comparing our findings with the theoretical predictions. Finally, in Sec. IV we display evidence for a strange attracting set above the homoclinic threshold. This numerical result is discussed briefly.

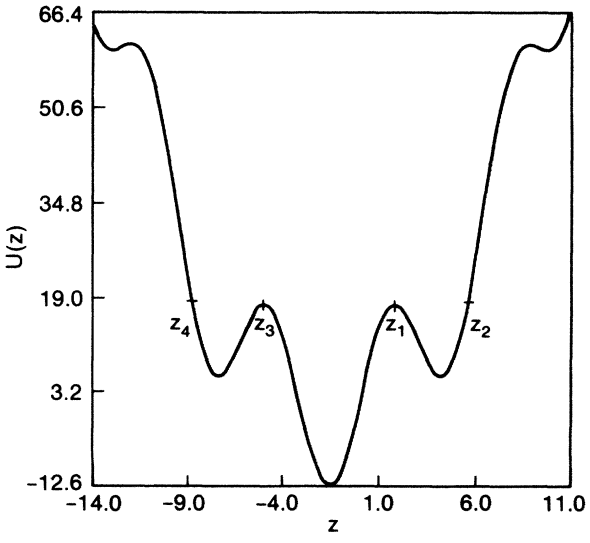

FIG. 1. Potential $U(z)$ vs z for $(\beta, \omega_0, x_0) \equiv (2, 1, 0)$.

II. APPROXIMATE ANALYTIC SOLUTION OF THE rf SQUID EQUATION

For the purpose of obtaining a separatrix solution, we now turn to Eq. (1.2) and formally integrate it, obtaining

$$\dot{z}^2 = v_i^2 + 2U(z_i) - 2U(z) , \tag{2.1}$$

where $(z_i, v_i = \dot{z}_i)$ are the initial values used to determine the integration constant. Equation (2.1) is now formally integrated to yield

$$I(z) - I(z_i) \equiv \left[\int_0^z - \int_0^{z_i}\right] \frac{dy}{[v_i^2 + 2U(z_i) - 2U(y)]^{1/2}} = \pm t , \tag{2.2}$$

where we select the negative sign in (2.2) since we shall always consider $z \le z_i$ (this choice of sign yields the

correct monotonic decreasing behavior on the separatrix).

In order to evaluate the integral in (2.2), we employ a polynomial approximation of the trignometric function in $U(z)$. Specifically, we set

$$\cos z \approx 1 - a_2 z^2 + a_4 z^4 , \tag{2.3a}$$

where $a_2 = 0.4967$ and $a_4 = 0.037\,05$. Such approximations have been derived[17] by expanding cosz in a continued fraction series that can be truncated at any order, depending on the level of accuracy desired. Differentiating (2.3a) we obtain

$$\sin z \approx a_1 z - a_3 z^3 , \tag{2.3b}$$

where $a_1 = 0.9934$ and $a_3 = 0.1482$. The above approximation (which may be extended to include higher-order terms for greater accuracy) has been estimated to yield an error of 0.13% or less in the computation of the trignometric functions. In applying these approximations, one is under the restriction $z \le \pi/2$. Hence, for $z > \pi/2$, the angle z must be expressed in terms of an equivalent angle in the first quadrant before computing the trignometric function. We shall demonstrate below how this spline approximation is implemented.

Let us assume, as an example, that $3\pi/2 \le z \le 2\pi$. We break the first integral in (2.2) into integrals over each of the quadrants [a similar procedure is followed for the second integral in (2.2)]:

$$I(z) \equiv \left[\int_0^{\pi/2} + \int_{\pi/2}^{\pi} + \int_{\pi}^{3\pi/2} + \int_{3\pi/2}^{z} \right] \times \frac{dy}{[v_i^2 + 2U(z_i) - 2U(y)]^{1/2}} . \tag{2.4}$$

The first three integrals on the right-hand side of (2.4) may be cast in the form

$$I_k \equiv \int_0^{\pi/2} \frac{d\theta}{[f_k(\theta)]^{1/2}}, \quad k = 1,2,3 \tag{2.5}$$

where $0 \le \theta \le \pi/2$ so that the expansions (2.3) are valid. Finally, the last integral on the right-hand side of (2.4) may be written as $I_4 - I_4(2\pi - z)$, where I_4 takes on the form of (2.5) (with $k = 4$) and $I_k(z)$ is given, in general, by an integral of the form (2.5) with the upper limit replaced by z. In using the expansions (2.3), it is necessary to transform the integrals in (2.4) so that the argument of the trignometric function is restricted to the first quadrant. This necessitates the breakup of the integral as above, with the integrand being redefined in each of the quadrants according to

$$f_1(\theta) \equiv v_i^2 + 2U(z_i) - \omega_0^2 \left[\theta + \frac{\pi}{2} \right]^2 - 4\pi\omega_0^2 \beta \sin\theta , \tag{2.6a}$$

$$f_2(\theta) \equiv v_i^2 + 2U(z_i) - \omega_0^2 \left[-\theta + \frac{3\pi}{2} \right]^2 - 4\pi\omega_0^2 \beta \sin\theta , \tag{2.6b}$$

$$f_3(\theta) \equiv v_i^2 + 2U(z_i) - \omega_0^2 \left[\theta + \frac{3\pi}{2} \right]^2 + 4\pi\omega_0^2 \beta \sin\theta , \tag{2.6c}$$

$$f_4(\theta) \equiv v_i^2 + 2U(z_i) - \omega_0^2 \left[-\theta + \frac{5\pi}{2} \right]^2 + 4\pi\omega_0^2 \beta \sin\theta . \tag{2.6d}$$

One readily observes that for any $0 \le z \le 2\pi$, the integral in (2.4) takes the form

$$I(z) = I_1 + I_2 + I_3 + I_4 - I_4(2\pi - z), \quad \frac{3\pi}{2} \le z \le 2\pi \tag{2.7a}$$

$$= I_1 + I_2 + I_3(z - \pi), \quad \pi \le z \le \frac{3\pi}{2} \tag{2.7b}$$

$$= I_1 + I_2 - I_2(\pi - z), \quad \frac{\pi}{2} \le z \le \pi \tag{2.7c}$$

$$= I_1(z), \quad 0 \le z \le \frac{\pi}{2} . \tag{2.7d}$$

The extension of the above procedure for $z > 2\pi$ is straightforward and will not be discussed here. We have thus reduced the integral (2.2) to a sum of integrals, each of which may be analytically evaluated using the approximations (2.3). For a general initial and final value of z, the integrals I are evaluated in terms of the Jacobian elliptic functions. On the separatrix, however, the solution simplifies considerably, as will be apparent in what follows. We might mention that had we solved the dynamic equation in its original form [Eq. (1.1)], the second term in (1.3) would have contained cos$x$, in which case we would have had to approximate it using (2.3a). The functions f_k appearing in (2.5) and (2.6) would then be quartics rather than the relatively simple cubics. The solution in this case, while still analytically tractable (and slightly more accurate), becomes extremely complicated; in particular, an analytic computation of the Melnikov function becomes impossible. This is the reason for making the phase transformation $x \to z$ which results in Eq. (1.2).

Before proceeding with the evaluation of the solution (2.2), we briefly consider the accuracy of the potential (1.3) in light of the approximation (2.3b). The sin$z$ term in (1.3) is replaced by $\sin(\pi - z)$ in the second quadrant, $-\sin(z - \pi)$ in the third quadrant, and $-\sin(2\pi - z)$ in the fourth quadrant. For $z > 2\pi$, the procedure is repeated. The expansion (2.3b) is then used to compute $U(z)$. In Table I we list the values of the turning point z_1 obtained directly from (1.6) and through use of the approximation (2.3) in (1.6). This is followed by a computation of the values of the potential $U(z_1)$ for each of these values of z_1, where we have used a combination of (2.3) and (1.3) to compute the approximate values of $U(z_1)$. Finally, the point z_2 is computed via the condition $U(z_1) = U(z_2)$, using, once again, the appropriate values of $U(z_1)$, corresponding to the direct and approximate [using (2.3)] calculations. The procedure is repeated for different β values with $(\omega_0, x_0) \equiv (1,0)$ throughout. This table highlights the deviations between the direct and approximate quantities, with the error introduced in the computation of the turning point z_1 appearing to increase with increasing β. This is due partly to the error inherent in numerically obtaining the turning points of the poten-

TABLE I. Parameters relevant to the separatrix calculations involving the potential $U(z)$ and its approximation using the expansion (2.3). $\omega_0=1, x_0=0$.

	z_1		$U(z_1)$		z_2	
β	Direct	Approximate	Direct	Approximate	Direct	Approximate
0.8	2.522 316 8	2.498 589 0	11.294 425 50	11.292 663 08	3.759 848 42	3.756 399 95
0.9	2.332 681 1	2.310 599 2	11.710 069 19	11.719 848 93	4.195 870 66	4.206 957 30
1.0	2.218 074 7	2.201 349 9	12.190 044 30	12.209 259 44	4.479 622 61	4.485 096 90
2.0	1.846 177 9	1.869 338 9	17.930 745 21	17.964 236 20	5.609 041 39	5.611 040 63
2.5	1.786 168 5	1.819 106 3	20.979 667 44	20.997 727 30	5.851 807 65	5.851 562 52

tial [through solving Eq. (1.6)], but also to the fact that the absolute error introduced into the calculation through the use of the approximations (2.3) increases with increasing nonlinearity.

A. Separatrix solution

We now turn our attention to the formal solution (2.2) and evaluate it explicitly on the separatrix. This is followed by an example using a representative set of system parameters. We assume that the particle starts at the point z_i $(=z_2)$ at time $t=0$ with zero initial velocity. It arrives at the point z_1 at $t=\infty$. We consider the case of moderate β $(\lesssim 1.5)$ for which the points z_1 and z_2 are one quadrant apart, although, as will be indicated later, the extension to higher β values is readily accomplished, albeit somewhat more tediously. Since the final point z is always contained in the second quadrant (for any value of β), (2.2) takes the form (noting that $\pi \le z_i \le 3\pi/2$)

$$I_3(z_i-\pi)+I_2(\pi-z)=t \ , \tag{2.8}$$

where we have used (2.7b) and (2.7c). Consider the function $f_2(z)$ appearing in the integral $I_2(\pi-z)$. This function is, generally, a cubic in z. On the separatrix, however, it may readily be seen that the function f_2 has only two roots, one of these roots being, in fact, a turning point. In other words, we may write, on the separatrix,

$$f_2(z)=A_2(z-|\alpha_1|)^2(z+|\alpha_3|) \ , \tag{2.9}$$

where $A_2=4\pi\beta\omega_0^2 a_3$. Here one sees that the z axis is tangential to the curve $f_2(z)=0$ at the point $z=|\alpha_1|$. In writing f_2 in the form (2.9), the *location* of the roots on the z axis is determined by the signs appearing in the factors on the right-hand side. We also have (from simple geometrical considerations)

$$z_i=\pi+|\alpha_3| \equiv z_2 \tag{2.10a}$$

and

$$z_1=\pi-|\alpha_1| \ . \tag{2.10b}$$

The integrals in (2.8) are now readily evaluated to yield

$$z(t)=z_i-\alpha\tanh^2\zeta t \ , \tag{2.11}$$

where $\alpha=z_2-z_1$ and

$$\zeta=(4\pi\omega_0^2\beta a_3\alpha)^{1/2}/2 \ .$$

Equation (2.11) is the solution of the dynamic equation (1.2) on the separatrix $(z_1 z_2)$, i.e., in the side well of the potential. One sees that as $t\to\pm\infty$, $z\to z_1$, and the stable and unstable manifolds are identical, as one might expect. Before continuing we must reiterate the fact that the special form of the solution (2.11) was derived for the case of moderate nonlinearity, for which the point z_2 is contained in the third quadrant. The symmetry between the solutions in the second and third quadrants [this symmetry is evident through a glance at equations (2.7b) and (2.7c)] allows us to write down the relatively simple expression (2.11). The foregoing analysis may also be applied to cases (involving larger β values) for which the points z_1 and z_2 are several quadrants apart. In these cases, however, the derivation of a solution analogous to (2.11) is not so simple. Specifically, one must compute the solution $z(t)$ quadrant by quadrant and systematically piece it together to obtain its complete behavior for all times. The solution is then a spline function.

Having computed the separatrix solution (2.11) it is instructive to compare it with the solution obtained via a direct numerical simulation of (1.2). In doing so we demonstrate some of the uncertainties endemic to a numerical computation of the separatrix solution. We consider as a specific example the case $(\beta,\omega_0,x_0)\equiv(1,1,0)$. Writing the cubic $f_2(z)$ in the form

$$f_2(z)\equiv A_2z^3+B_2z^2+C_2z+D_2 \ , \tag{2.12}$$

we obtain, through comparison with (2.6b),

$$(A_2,B_2,C_2,D_2)\equiv(1.862\,34,-1,-3.058\,65,2.211\,91) \ ,$$

where we have used the approximate values of z_1, z_2, and $U(z_1)$ from Table I [since the approximation (2.3) is contained in the analytic integration of (2.2)]. A direct numerical computation of the roots of the cubic (2.12) yields three roots, two of which lie very close to each other. This uncertainty is displayed in Fig. 2, which shows a plot of the function $f_2(z)$. The point $z=\alpha_1$ at which the curve touches the z axis is not uniquely determined, pointing out a source of error inherent in the direct numerical computation of the roots. Such a numerical computation yields the roots $a_1=0.940\,23+0.001\,42i$, $\alpha_2=0.940\,23-0.001\,42i$, and $\alpha_3=1.343\,386$. It is apparent, therefore, that even though the approximate values of z_1, z_2, and $U(z_1)$ were used in the computation of the coefficients of the cubic (2.12), numerically solving the cubic yields quantities that are different from those that were input into the coefficients of the cubic in the first place. The roots α_1 and α_2 coincide if one ignores their small imaginary parts (the existence of these imaginary parts may be directly attributed to errors inherent in

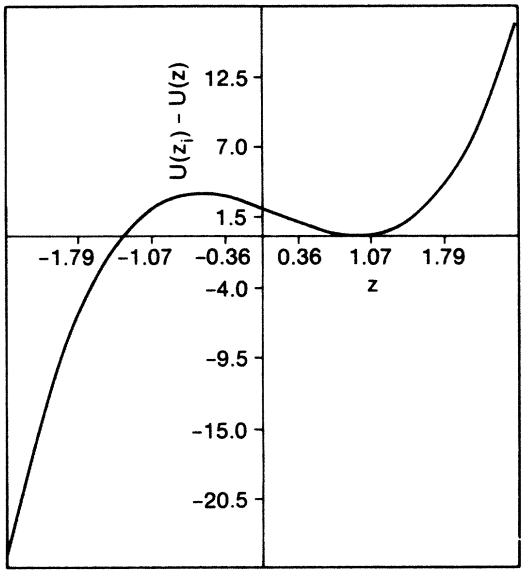

FIG. 2. Difference $U(z_i)-U(z)$ on the separatrix. $(\beta,\omega_0,x_0)\equiv(1,1,0)$.

the numerical computation of these roots); the resulting root represents the turning point at which the curve of Fig. 2 touches the z axis. In Fig. 3 we plot the solution $z(t)$ on the separatrix for the special case under consideration in this paragraph. The solid curve corresponds to the solution obtained via a direct numerical integration of the differential equation (1.2). In carrying out this integration, the direct values of z_1 and z_2 used are from Table I. The approximate analytical solution (2.11) is also plotted in this figure (dotted curve). It is evident that although the behavior of the two solution curves is very close, there are differences, most notably at long times (as

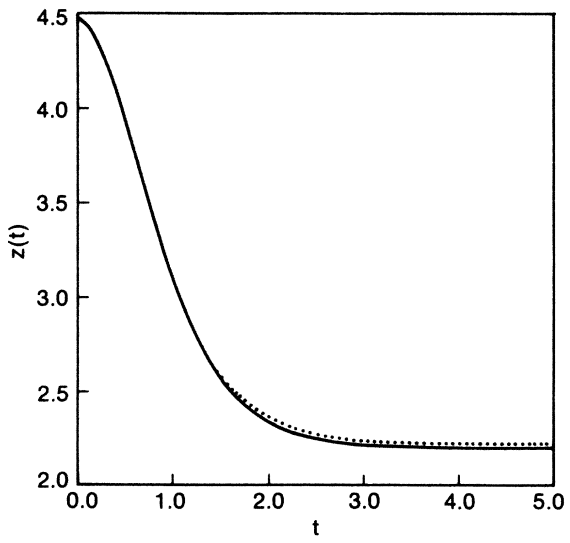

FIG. 3. Solution $z(t)$ [Eq. (2.11)] in side well for $\beta=1$. The dotted curve represents Eq. (2.11) and the solid curve is obtained by direct (numerical) integration of (1.2).

one would expect from Table I). It is certainly true that in addition to the approximations associated with the solution (2.11), tolerance-related errors may be introduced via the numerical simulation of Eq. (2.1). These latter errors are more difficult to estimate.

B. Off-separatrix solution

The treatment of Sec. II A may be modified and extended to cover the case when the initial value z_i does not correspond to the point z_2. Once again we utilize the polynomial approximation (2.3) in evaluating the integral (2.2). However, the initial velocity must be taken to be nonzero. As in Sec. II A the integral in (2.2) is broken up into the sum of separate integrals over the four quadrants. In this general case, however, the cubic f_k will have three distinct roots (two of which may be complex conjugates of each other). Our treatment in this section is brief since we are not concerned with the off-separatrix solution in the rest of this work. The procedure, however, is worth outlining since it may be of practical interest.

Let us assume that the initial position z_i and initial (nonzero) velocity v_i are arbitrarily chosen at $t=0$. At any later time, the position $z(t)<z_i$ may be written down, using (2.2), (2.4), and (2.7), as

$$I(\bar{z}_i)-I(\bar{z})=t\ , \tag{2.13}$$

where $\bar{z}$ takes on the values z, $\pi-z$, $z-\pi$, or $2\pi-z$, depending on the quadrant of location of z (the cubic f_k appearing in the integrand of I must also be suitably selected). We now assume that the cubic $f_k(z)$ has three distinct roots $\alpha_{k1}>\alpha_{k2}>\alpha_{k3}$, where k defines the quadrant of location of the point z. Then one may write (2.13) in the form

$$I(\bar{z})\equiv\int_0^{\bar{z}}\frac{d\theta}{[f_k(\theta)]^{1/2}}=\zeta_1 t+\zeta_2\ , \tag{2.14}$$

where

$$\zeta_k=2\left[\frac{A_{k2}}{\alpha_{k1}+\alpha_{k3}}\right]^{1/2}$$

(A_{k2} being the coefficient of z^3) and ζ_2 is a constant to be determined by the initial condition. The integral $I(\bar{z})$ is an elliptic integral of the first kind and one may cast (2.14) in the form

$$\bar{z}(t)=\alpha_{k3}+\frac{\alpha_{k1}-\alpha_{k3}}{\mathrm{sn}^2(\zeta_1 t+\zeta_2)}\ , \tag{2.15}$$

where sn is the elliptic function of Jacobi and the initial condition enables us to set the constant ζ_2 via the condition

$$\mathrm{sn}\zeta_2=\left[\frac{\alpha_{k1}-\alpha_{k3}}{\bar{z}_i-\alpha_{k3}}\right]^{1/2}\ . \tag{2.16}$$

In practice, it is often more convenient to evaluate the Jacobian elliptic functions in terms of their inverses, i.e., to evaluate $I(\bar{z})$ directly in terms of the elliptic integrals of the first kind. Then one may write (2.15) in the equivalent form,

$$t=\zeta_1^{-1}[F(\tilde{\phi}\,|\,m_k)-F(\tilde{\phi}_i\,|\,m_{k_i})]\ , \tag{2.17}$$

where we have set

$$\tilde{\phi}\equiv\left[\frac{\alpha_{k1}-\alpha_{k3}}{\bar{z}-\alpha_{k3}}\right]^{1/2}$$

and F is the elliptic integral of the first kind having amplitude m_k, the latter quantity being expressed in terms of the roots of the cubic f_k. The techniques for the evaluation of these integrals are well known[18] and will not be repeated here.

III. THE MELNIKOV FUNCTION FOR THE rf SQUID

We now suppose that the unperturbed system discussed in Sec. II is perturbed by a combination of dissipative and periodic forces, i.e., F_k and F_ω, defined in Eqs. (1.4) and (1.5), respectively. The purpose of this section is to theoretically investigate the condition for the onset of homoclinic behavior in the presence of the above perturbations.

The Melnikov test function may be written as,[3–5,7]

$$\Delta(t_0)\equiv\int_{-\infty}^{\infty}[F_k(t)+F_\omega(t)]\dot{z}(t)dt\equiv\Delta_k+\Delta_\omega(t_0)\ . \tag{3.1}$$

This remarkable test function, valid under weak perturbation,[7] has the following properties: (a) $\Delta(t_0)\equiv 0$ for no perturbation and (b) $\Delta(t_0)$ changes sign (as a function of t_0), indicating a crossing of the stable and unstable manifolds, i.e., the presence of a *homoclinic point*. As discussed in Sec. I, this indicates the presence of a Cantor set structure or homoclinic instability.[2,5] The simplicity of this procedure arises from the fact that the quantity $\dot{z}(t)$ in (3.1) is the *unperturbed* separatrix velocity in the region (z_1z_2), given approximately by the time derivative of Eq. (2.11). This arises because the separatrix orbits are, in a sense, the most sensitive to any perturbation. The Melnikov function can only be applied to separatrix orbits. No analysis has been carried out for nonseparatrix orbits and thus it is applicable only to unperturbed nonlinear oscillators with a hyperbolic fixed point and a separatrix. The rf SQUID is a good example. In applying the Melnikov function to the rf SQUID, considerable care must be taken to ensure that the magnitudes of the parameters β, k, A, etc. or combinations of these parameters fall within the realm of validity of perturbation theory.

Let us now evaluate the integrals in (3.1), considering first the region (z_1z_2) of the potential (1.3) (see Fig. 1). Using the solution (2.11) (we are, once again, confining ourselves to the moderate β case), we readily obtain the first integral as

$$\Delta_k=\tfrac{16}{15}\alpha^2\zeta k\ , \tag{3.2}$$

where the quantities α and ζ have been defined in connection with Eq. (2.11). In order to evaluate the second integral in (3.1) we express it as the sum of two integrals:

$$\Delta_\omega(t_0)\equiv-2\alpha\zeta A\int_{-\infty}^{\infty}\tanh\zeta t\,\mathrm{sech}^2\zeta t(\sin\omega t\cos\omega t_0-\cos\omega t\sin\omega t_0)dt\ . \tag{3.3}$$

Noting that $\dot{z}(t)$ is an odd function in the side well of the potential, the above integral becomes

$$\Delta_\omega(t_0)=-4\alpha\zeta A(\cos\omega t_0)\int_0^{\infty}\tanh\zeta t\,\mathrm{sech}^2\zeta t\,\sin\omega t\,dt\ . \tag{3.4}$$

This integral is readily evaluated to give

$$\Delta_\omega(t_0)=-\frac{4\pi\omega^2A\cos\omega t_0}{A_2\sinh[\pi\omega/(A_2\alpha)^{1/2}]}\ , \tag{3.5}$$

where the quantity A_2 has been defined in connection with Eq. (2.9). It is evident that the function Δ_ω has its extrema for $\cos\omega t_0=\pm1$ [all other quantities in (3.5) being fixed]. In the presence of finite damping one obtains homoclinic behavior above a critical threshold, which may be found by setting $\Delta_k=|\Delta_\omega(t_0)/\cos\omega t_0|$. This condition leads one to the threshold condition for the onset of homoclinic behavior,

$$\frac{A}{k}=\frac{2}{15\pi}\frac{\alpha^{5/2}A_2^{3/2}}{\omega^2}\sinh[\pi\omega/(A_2\alpha)^{1/2}]\ . \tag{3.6}$$

A similar result was first obtained by Holmes[4] for the anti-Duffing oscillator. Damping may suppress chaos; in this case, the forward manifold spirals from the hyperbolic fixed point into the elliptic fixed point, while the backward manifold spirals outward; the manifolds do not cross. As mentioned in Sec. I, an analysis similar to that just carried out has been done for the simple Josephson junction.[7–10] The analysis in that case is considerably simplified by the fact that the term linear in x in Eq. (1.1) is absent from the Josephson-junction dynamics, and the unperturbed solution may be obtained analytically without the approximations of Sec. II. Unlike the rf SQUID, the Josephson junction is described by a potential in which all the wells have the same size; in fact, the potential in this case is simply of the form $U(z)\approx\sin z$. For the system under consideration in this work, one recovers, qualitatively, the features of the Josephson junction in the limit $\beta\to\infty$ (in this limit, all the wells in the potential of Fig. 1 approach the same size). In what follows we shall compare the results of this section with existing results for the Josephson junction.

In Fig. 4 we plot the quantity $|\Delta_\omega(t_0)/\cos\omega t_0|$ as a function of the driving frequency ω for $\beta=1$ in the side well $(z_1\le z\le z_2)$ of Fig. 1. The natural frequency ω_0 is set equal to unity in this plot. The constant quantity Δ_k of Eq. (3.2) is also shown (the straight line). The solid curve is obtained by numerical evaluation of the integral in (2.2) and a subsequent numerical computation of the Melnikov integral (3.4). Also shown are data points corresponding to the theoretical result obtained from (3.5).

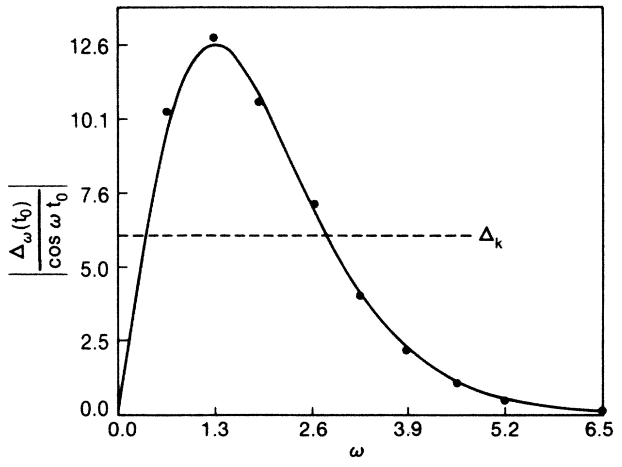

FIG. 4. Melnikov function amplitude in the side well (z_1z_2). The solid curve represents numerical calculation and data points are derived from Eq. (3.5). The dashed line represents Eq. (3.2). $(\beta,k,A)\equiv(1,1,4)$.

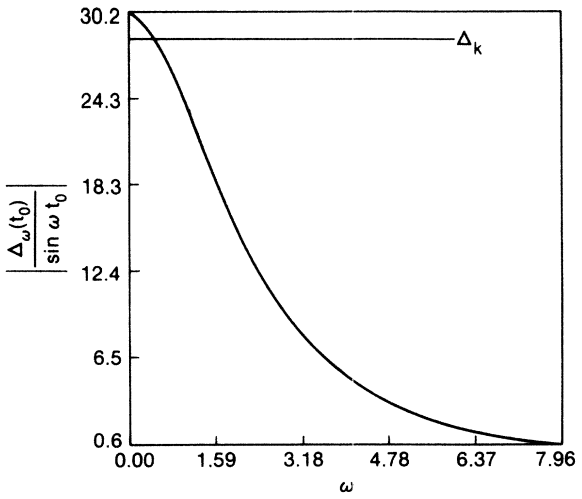

FIG. 5. Melnikov function amplitude in the center well (z_1z_3) for the same parameter values as Fig. 5. Both curves are obtained numerically.

Note that the difference between a numerical calculation of Δ_k and the theoretical result (3.2) is much smaller than the scale of this figure. For the moderate value of β used in this figure, the agreement between theoretical and numerical results is quite good. We reiterate that the numerical computations are not totally accurate; however, it is difficult to obtain realistic estimates of the error introduced into the numerical integrations of Eqs. (2.2) and (3.4). The intersection of the straight line with the curve represents the threshold for the onset of homoclinic behavior since the Melnikov function changes sign as one crosses the line. The graph of $|\Delta_\omega(t_0)/\cos\omega t_0|$ is peaked at $\omega=\omega_c$, given [for the theoretical result (3.5] by

$$\omega_c = 1.915\frac{(A_2\alpha)^{1/2}}{\pi} . \tag{3.7}$$

This peak represents the minimum value of (A/k) necessary for the onset of homoclinic behavior. For $\beta=1$ one obtains the critical values $(\omega, A/k)\equiv(1.257,1.79)$ from the theoretical calculations. These numbers compare quite favorably with the values (1.26,1.78) obtained via the numerical calculations.

Figure 5 shows the quantity $|\Delta_\omega(t_0)/\sin\omega t_0|$ for the center well of the potential (1.3) (i.e., $-\pi-z_1\le z\le z_1$) corresponding to the separatrix (z_1z_3) of Fig. 1. For the rf SQUID we expect the results in the center well to differ from those obtained in the side well, both because of the difference in well dimensions and the difference in the parity of the velocity between the wells (both these features are absent in the Josephson junction). This figure has been obtained numerically. If one considers the velocity profiles in the two wells (Fig. 6), it is seen that the velocity in the side well is odd. Hence, in (3.3), only the first term contributes to the integral which is peaked as some nonzero frequency ω_c; this corresponds to the case worked out analytically in this section. In the center well, however, the velocity is even so that the Melnikov integral in this case is proportional to $\sin\omega t_0$ in agreement with results derived for the Josephson junction.[7–11] In Fig. 7 we show the critical (i.e., minimum) value $(A/k)_c$ as a function of the nonlinearity parameter β, where the subscript c implies that we have evaluated (A/k) at the critical frequency ω_c corresponding to the side well. Results for the center as well as the side well of the potential, are plotted. As expected, when a greater disparity exists in the relative dimensions of the wells (for moderate β), a higher minimum value of (A/k) is required to trigger homoclinic behavior in the center well at the critical driving frequency ω_c corresponding to the side well. For large β values, the values of $(A/k)_c$ in the two wells converge.

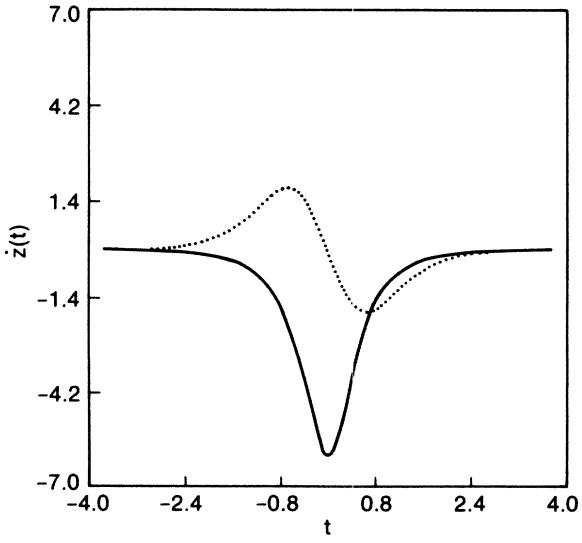

FIG. 6. Velocity profile $\dot{z}(t)$ in the center well (solid curve) and in the side well (dotted curve). $\beta=1$.

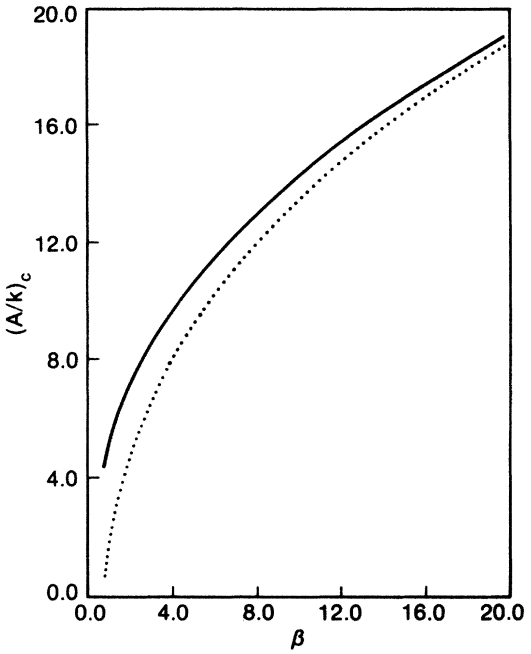

FIG. 7. Critical values of (A/k) as a function of β in center well (solid curve) and side well (dotted curve). Both curves are derived numerically at the critical frequency ω_c corresponding to the peak of the Melnikov function amplitude in the *side* well.

IV. HOMOCLINIC THRESHOLD AND "STRANGE" ATTRACTOR (NUMERICAL)

In this section we will show Poincaré return maps of the numerical solutions to the driven damped rf SQUID, Eqs. (1.2)–(1.5). The objective will be to first estimate the onset of homoclinic crossing and compare the results with those of Sec. III. This was first done by Holmes[4] for a cubic map, which preserved some of the properties of the anti-Duffing oscillator. No such results have previously been obtained for the Josephson junction or the rf SQUID. In the final part of this section we will give evidence for the existence of a strange attracting set in the solutions, which develops in a parameter range beyond the onset of the homoclinic instability.[5] Such attractors have been numerically studied in detail for the Josephson junction (see Ref. 8 for a review).

Comments are made by Holmes[4] concerning numerical techniques, but it is worthwhile to also comment here on the procedure and the difficulties. In order to facilitate the numerical integration of the differential equation (1.1) we have introduced the scaled time variable $\tau \equiv \omega_0 t$. It is apparent that for the special case ω_0 considered throughout this work, this scaling does not change the original equation at all. However, in all practical applications of rf SQUID's, one usually has $\omega_0 \approx 10^{10}$, which leads to enormous problems when one attempts to integrate the equation of motion (1.1), unless such a scaling is utilized. The stable and unstable manifolds discussed in this section are computed by mapping a large number of points on the stable (unstable) manifold near the saddle point, one or more Poincaré periods backward (forward). In the presence of damping and the periodic external perturbation one is faced with the problem of computing the saddle point. Although numerous methods exist for this purpose (e.g., averaging[5,19] and harmonic balance[19]), the answer obtained for the form of the nonlinearity in this problem is not accurate enough. Nevertheless, by estimating the location of the saddle point and mapping a small area around this point forward and backwards in time [using Eq. (1.1)], one obtains a reasonably good picture of these manifolds and their behavior relative to each other. In order to obtain clear and distinct pictures of the manifolds, one must make the mapped area (about the saddle point) arbitrarily small. In the system at hand, however, one cannot do this since the saddle point has not been accurately located. This uncertainty is most likely the reason for the smearing of the manifolds in Figs. 8–13. It is also possible that some numerical uncertainties arise because it is difficult for the integrating routine to exactly follow the true solution of the differential equation so close to an unstable fixed point.

Let us now consider some results. We will take $(\beta,\omega,k) \equiv (2,2.25,1)$ (the value $\omega = 2.25$ is chosen because it is very close to critical frequency ω_c for this value of the nonlinearity) and vary the driving amplitude. We set $q \equiv A/2\pi$ and note that throughout this section we work in the original system of variables $(x,\dot{x},t)$ of Eq. (1.1). For $q = 0.5$ shown in Fig. 8, the unstable hyperbolic fixed point is close to the unperturbed hyperbolic point $x = 0.5438$ (this point corresponds to the point z_1 in Table I). A branch of the unstable manifold spirals into the right-hand elliptic fixed point due to the dispersion $(k = 1)$. A branch of the stable manifold emanates from the region of the center well and approaches the hyperbolic point "around" the unstable solution in the Poincaré phase plot; the stable and unstable manifolds do not touch. This pattern is characteristic of an overdamped system. For $q = 0.72$ shown in Fig. 9, the unstable manifold approaches the stable manifold by developing a sharp cusp. At $q = 0.73$ (Fig. 10) the manifolds appear to touch, and in Fig. 11 they have already crossed, for

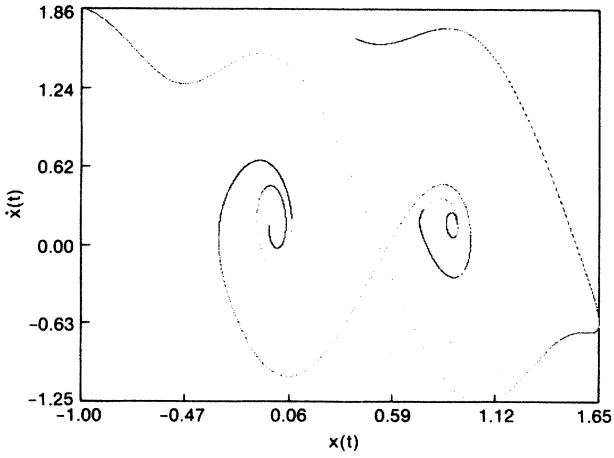

FIG. 8. Stable and unstable manifolds in parameter regime where no homoclinic behavior is expected. $(\beta,\omega,k,q = A/2\pi) \equiv (2,2.25,1,0.5)$.

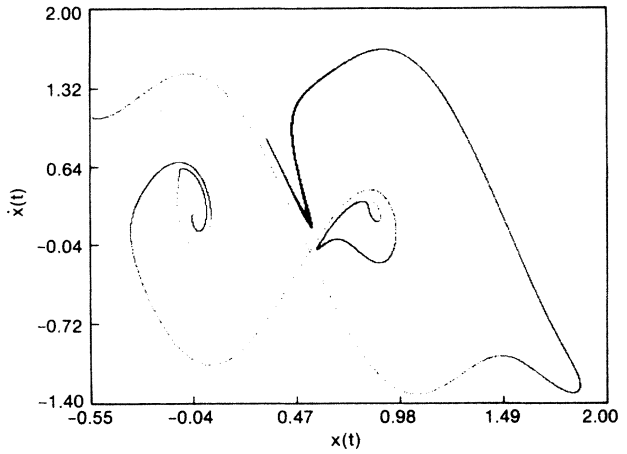

FIG. 9. Same as Fig. 8 but with $q=0.72$. The stable manifold has developed a cusp and is approaching the unstable manifold in the side well.

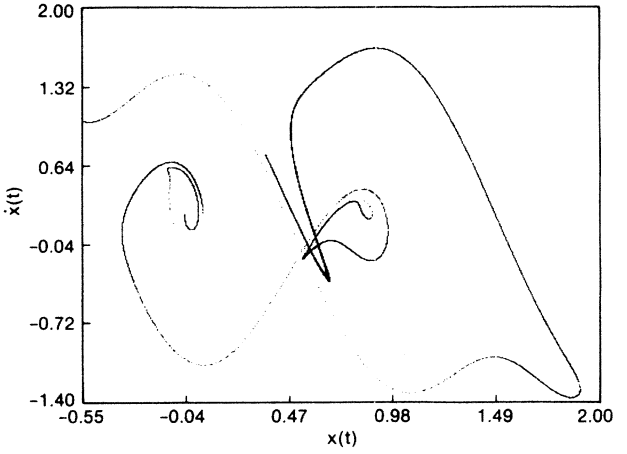

FIG. 11. Same as Fig. 10 but with $q=0.75$. Supercritical case; a homoclinic crossing has taken place in the side well.

$q=0.75$, in the side well. For these parameter values, the Melnikov function of Sec. III predicts a homoclinic crossing for $q=0.74$, in good agreement (considering the numerical difficulties) with our numerical results. Further increasing q causes the other branch of the stable manifold to loop back and cross the other branch of the unstable manifold; the latter is attracted to the stable (elliptic) fixed point in the center well. Figure 12 shows the near crossing for $q=1.21$, and in Fig. 13 the homoclinic intersection has already occurred (for $q=1.25$). The Melnikov function predicts the first crossing in the center well for these parameters at $q=1.2$.

Now let us turn to the evidence for the appearance of a global steady chaotic attracting set in the SQUID—a strange attractor. Chaos in such a set may be properly characterized by its Lyapunov exponent.[5,20] In Fig. 14 we plot the maximal Lyapunov exponent λ_m as a function of the periodic driving amplitude q with $(\beta,\omega_0,k)\equiv(2,1,1)$. This quantity was computed using the algorithm of Wolf *et al.*[21] It is evident that the system displays chaotic behavior (characterized by a positive λ_m) at a value of q somewhat above the homoclinic threshold value $q=1.21$. Further, one observes bands of periodic behavior (characterized by a negative λ_m) at higher q values. Such intermittent behavior is now known to occur in many nonlinear chaotic systems and, in particular, in the driven Duffing oscillator.[4]

We should comment that there is no theoretical connection between to the appearance of these attracting sets and what we have termed homoclinic instability. The Melnikov function does not characterize the appearance of a strange attractor, as is well known.[5] There have been efforts to correlate the Melnikov test empirically with the

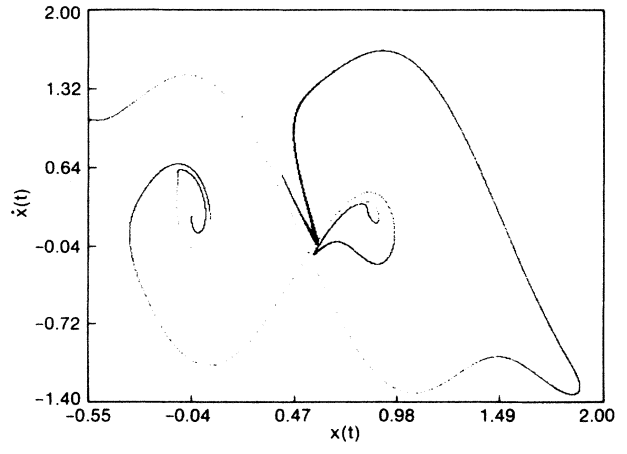

FIG. 10. Same as Fig. 9 but with $q=0.73$. Critical case; the manifolds just touch in the side well.

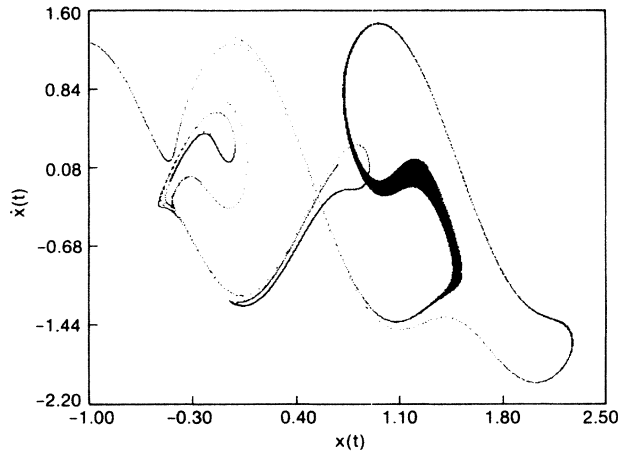

FIG. 12. Same as Fig. 11 but with $q=1.21$. Near-critical case for homoclinic crossing in the center well; the manifolds are about to touch in the center well (upper left of figure). For this value of q, homoclinic crossing has already occurred in the side well. The blackened area represents the smearing of the manifold due to the numerical uncertainties referred to in the text.

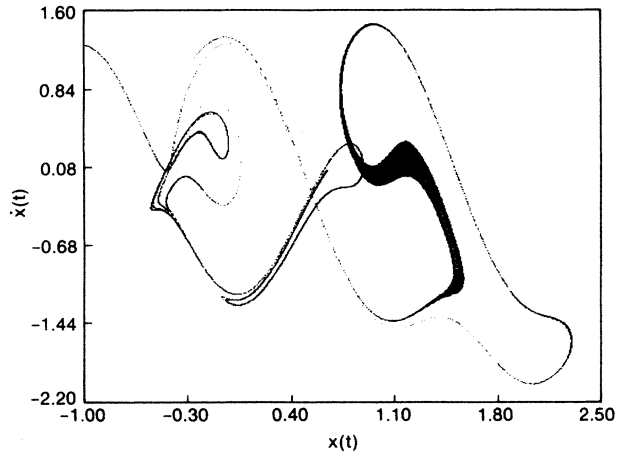

FIG. 13. Same as Fig. 12 but with $q=1.25$. Supercritical case; homoclinic crossing has just occurred in center well.

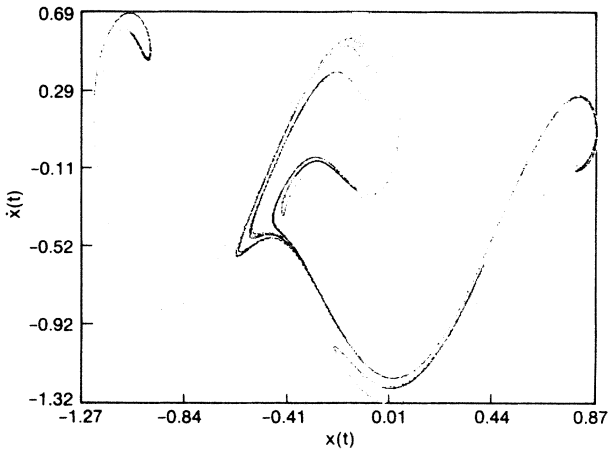

FIG. 15. Attractor corresponding to $q=1.43$, $k=1.0$. This case represents the possible onset of a chaotic attractor.

appearance of "chaos" in the Josephson junction.[8–11] While not uninteresting, they do not evidence a physical prelude or early scenario to the appearance of a strange attractor. At best, now, one would expect that the Melnikov function is a "rule of thumb" insofar as the appearance of a strange attractor is concerned. It provides one with a lower bound for the chaos threshold in a given nonlinear system and its vanishing should be considered a necessary condition for the appearance of chaos in the dynamics under consideration. Moon and Li[22] have constructed the fractal basin boundary for the driven anti-Duffing oscillator and have observed that the fractal structure appears to be correlated with the appearance of homoclinic orbits in this system. They observe that above the homoclinic threshold (determined by Holmes[4] using the Melnikov integral), the fractal basin boundary becomes quite complicated, whereas it is smooth and nonfractal below this threshold. They conclude that the Melnikov criterion is a necessary condition for the appearance of the complicated fractal boundary. Similar boundaries have been constructed for the driven damped pendulum (this is the mechanical analog of the Josephson junction) by Gwynn and Westervelt.[23]

We now examine the parameter range for which a chaotic steady attractor seemingly occurs. At any given time, the state of the system is completely specified through a determination of its position and velocity $(x,\dot{x})$. It is well known that in the chaotic regime, a Poincaré plot of the system evolution displays a strange attractor, i.e., there exist steady areas in state space to which the states of the system are preferentially attracted in a seemingly random manner—the successive values of $(x,\dot{x})$ jump from one region of state space to another in a random manner producing a topologically complex Poincaré section.

In Fig. 15 we show the Poincaré plot of the system for $q=1.43$, $k=1.0$; Fig. 16 shows the effects of reducing the damping to $k=0.3$ (the attractor displays a far more intricate structure at this lower k value). The value $q=1.43$ is seen (from Fig. 14) to be quite close to the threshold for the onset of chaos in this system. The (common logarithms of the) power spectral densities cor-

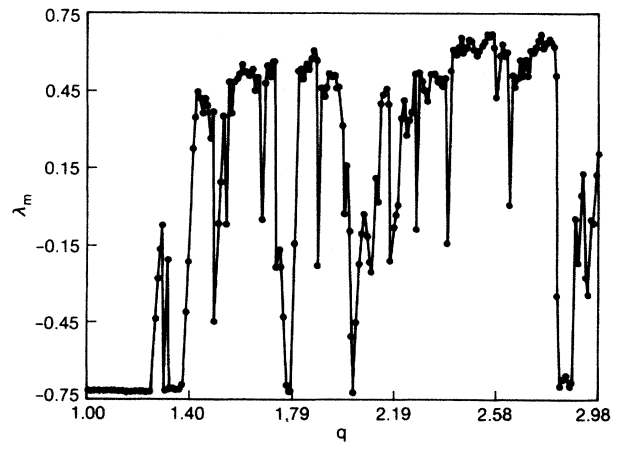

FIG. 14. Maximal Lyapunov exponent λ_m as a function of the driving force amplitude q. $(\beta,\omega,k)\equiv(2,2.25,1)$.

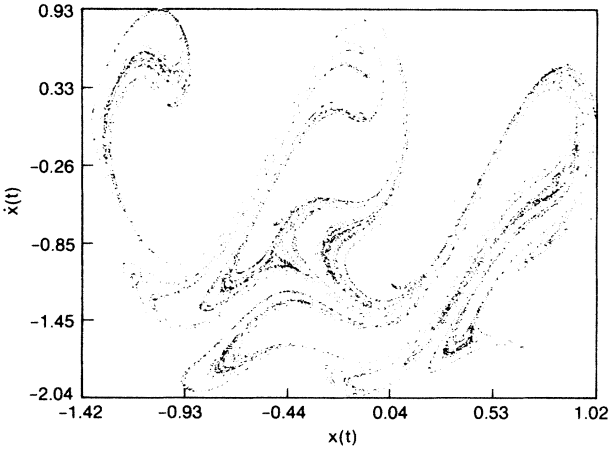

FIG. 16. Chaotic attractor corresponding to $q=1.43$, $k=0.3$.

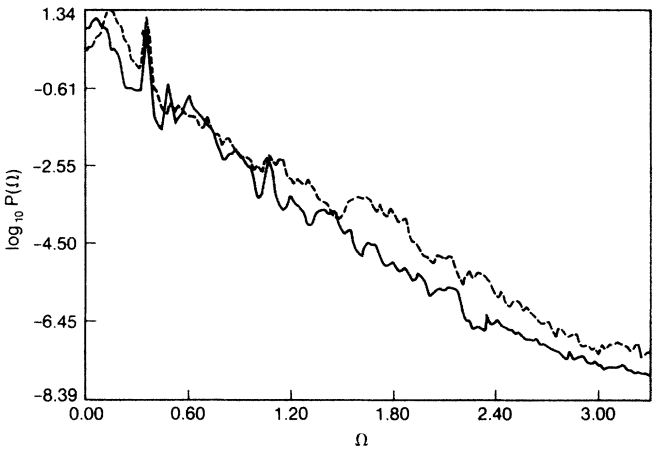

FIG. 17. Spectral densities corresponding to the attractors of Figs. 15 (solid curve) and 16 (dashed curve). Only the harmonics of the driving frequency are present, with the prominent peak on the left occurring at the fundamental driving frequency $\omega/2\pi=0.36$.

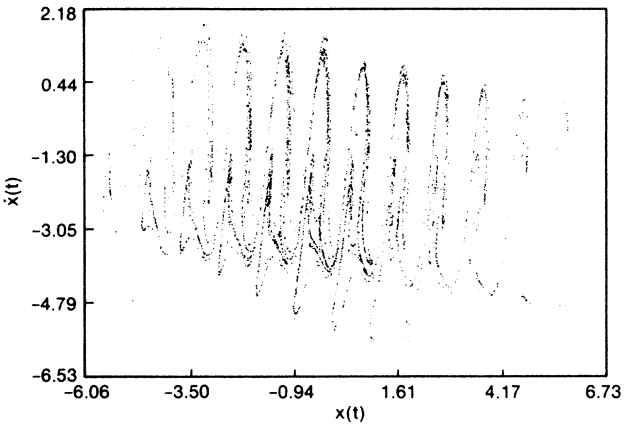

FIG. 18. Chaotic attractor for $(\beta,\omega,k,q)\equiv(15,2.25,1.5,21)$. The system makes excursions to numerous side wells.

responding to these cases are plotted in Fig. 17, with the power spectral density defined by

$$P(\Omega)=\left\langle \left| \frac{1}{T}\int_{-T/2}^{T/2} x(t)\exp(i\Omega t)dt \right|^2 \right\rangle , \tag{4.1}$$

where $T\rightarrow\infty$ and the angular brackets denote the time average (the spectra were computed over 1000 rf cycles with a frequency resolution of approximately 0.021 Hz). We observe that the power spectra contain harmonics of the driving frequency ($\omega/2\pi=0.36$) only, superimposed on a broadband noise background; this is a characteristic of chaotic behavior. Finally, in Fig. 18, we show a case in which the system is driven enough strongly so that it makes excursions to numerous side wells in the potential. The parameters used in this case are $(\beta,\omega,k,q)\equiv(15,2.25,1.5,21)$. The attractor displays a quasiperiodic overall structure.

In concluding, it is worthwhile to speculate on the significance of the frequency ω_c defined in (3.7). From (3.6) one observes that for a given damping k, the periodic force amplitude A necessary to trigger homoclinic behavior is a minimum for this value of the periodic driving frequency. Huberman *et al.*[24] have examined the appearance of chaos in the sinusoidally driven Josephson junction as a function of the driving frequency ω of the external signal. They observe chaotic behavior over a band of driving frequencies centered about $\omega\approx\omega_J/2$, where ω_J is the plasma frequency of the junction. Ritala and Salomaa[15] have observed the appearance of subharmonic and chaotic solutions in the rf SQUID in a band of frequencies centered about $\omega\approx\omega_r/2$. Here, ω_r is the resonance frequency that governs low-amplitude oscillations in the rf SQUID and is easily shown to be given by $\omega_r^2=\omega_0^2(1+2\pi\beta)$. The quantity ω_r may be considered the analog of the plasma frequency for the rf SQUID. It is interesting to note that as β is varied, the ratio ω_c/ω_r appears to lie in the interval [0.4,0.9] for moderate β ($0.74\leq\beta\leq100$). Hence, one might expect that setting the driving frequency ω approximately equal to the optimum value ω_c predicted by the Melnikov function might provide a connection between our results and earlier work.[15,18] Of course it must be remembered that simply selecting an appropriate driving frequency according to the above "prescription" is not, by itself, sufficient to induce homoclinic behavior or chaos in the system; the values of the damping coefficient k and the driving force amplitude A must also be appropriately selected.

ACKNOWLEDGMENTS

W.C.S. would like to thank the Alexander von Humboldt Society for making possible a sabbatical leave at the Max Planck Institute for Quantum Optics, Garching, Federal Republic of Germany, during which time this work was finished. A.R.B. and E.W.J. were supported by the U.S. Office of Naval Research through the Internal Research Program at the Naval Ocean Systems Center.

*Permanent address: Physics Department, University of Texas, Austin, TX 78712.

[1]H. Poincaré, *New Methods of Celestial Mechanics* (Gauthier-Villars, Paris, 1899), Vol. 3, p. 391.

[2]J. Moser, *Stable and Random Motions,* (Princeton University Press, Princeton, NJ, 1973).

[3]V. Melnikov, Trans. Mosc. Math. Soc. **12**, 1 (1963).

[4]P. Holmes, Philos. Trans. R. Soc. London, Ser. A **292**, 419 (1979).

[5]J. Guckenheimer and P. Holmes, *Nonlinear Oscillations, Dynamical Systems and Bifurcations of Vector Fields,* (Springer-Verlag, New York, 1983).

[6]V. Arnold, Dokl. Akad. Nauk SSSR **156**, 9 (1964) [Sov. Phys.—Dokl. **5**, 581 (1964)].

[7]J. Sanders, Celest. Mech. **28**, 171 (1982).
[8]R. Kautz and R. Monaco, J. Appl. Phys. **57**, 875 (1985).
[9]R. Kautz and J. Macfarlane, Phys. Rev. A **33**, 498 (1986).
[10]Z. Genchev, Z. Ivanov, and B. Todorov, IEEE Trans. Ciruits. Syst. **CAS-30**, 633 (1983).
[11]V. Gubankov, S. Zyglin, K. Konstantinyan, V. Koshelets, and G. Ovsyannikov, Zh. Eksp. Teor. Fiz. **86**, 343 (1984) [Sov. Phys.—JETP **59**, 198 (1984)].
[12]A. Bulsara, J. Appl. Phys. **60**, 2462 (1986).
[13]I. Dmitrenko, D. Konotop, G. Tsoi, and V. Shnyrkov, Fiz. Zizk. Temp. **9**, 666 (1983) [Sov. J. Low Temp. Phys. **9**, 340 (1983)].
[14]A. Smith, R. Sandell, A. Silver, and J. Burch (unpublished).
[15]R. Ritala and M. Salomaa, Phys. Rev. B **29**, 6143 (1984).
[16]R. Barrone and G. Paterno, *Physics and Applications of the Josephson Effect* (Wiley, New York, 1982).
[17]B. Carlson and M. Goldstein, Los Alamos Report No. LA-1943, 1955 (unpublished).
[18]G. Moretti, *Functions of a Complex Variable* (Prentice-Hall, Englewood Cliffs, NJ, 1964).
[19]C. Hayashi, *Nonlinear Oscillations in Physical Systems* (Princeton University Press, Princeton, NJ, 1985).
[20]A. Lichtenberg and M. Lieberman, *Regular and Stochastic Motion* (Springer-Verlag, New York, 1982).
[21]A. Wolf, J. Swift, H. Swinney, and J. Vastano, Physica **16**, 285 (1985).
[22]F. Moon and G. Li, Phys. Rev. Lett. **55**, 1439 (1985).
[23]E. Gwynn and R. Westervelt, Phys. Rev. Lett. **54**, 1613 (1985).
[24]B. Huberman, J. Crutchfield, and N. Packard, Appl. Phys. Lett. **37**, 750 (1980).